# Atomistic simulations, meso-scale analyses and experimental validation of thermal properties in ordinary Portland cement and geopolymer pastes

Antonio Caggiano [a,*], Ignacio Peralta [b,c,d], Víctor D. Fachinotti [b], Guido Goracci [e], Jorge S. Dolado [e,*]

[a] DICCA - Dipartimento di Ingegneria Civile, Chimica e Ambientale, Università degli Studi di Genova, via Montallegro 1, 16145 Genova, Italy
[b] Centro de Investigación de Métodos Computacionales (CIMEC), Universidad Nacional del Litoral (UNL)/ Consejo Nacional de Investigaciones Científicas y Técnicas (CONICET), Predio CONICET "Dr. Alberto Cassano", Colectora Ruta Nac. 168 km 0, Paraje El Pozo, CP 3000 Santa Fe, Argentina
[c] Laboratorio de Flujometría (FLOW), Facultad Regional Santa Fe (FRSF), Universidad Tecnológica Nacional (UTN), Lavaise 610, 3000 Santa Fe, Argentina
[d] Institut für Werkstoffe im Bauwesen, Technische Universität Darmstadt, Germany
[e] Centro de Física de Materiales, Centro Mixto CSIC-UPV/EHU, Paseo Manuel Lardizabal 5, 20018 San Sebastián, Spain

## ARTICLE INFO

## ABSTRACT

Ordinary Portland Cement (OPC)- and alternative binder-based materials have been widely used in Thermal Energy Storage (TES) applications due to their excellent TES capacities, good mechanical properties and low-cost. In this attempt, this work proposes an upscaling procedure to model the TES properties of two hydrated pastes made of OPC and a Hybrid cement (i.e., an alternative H-Cement binder), the latter employed for a GEOpolymer-based composite (GEO). Firstly, an atomistic approach based on energy minimization and molecular dynamics is employed for modelling the thermal behaviors and heat storage capacities of CSH (calcium silicate hydrate) and NASH (sodium aluminosilicate hydrate) phases, being those the main phases for OPC-based paste and GEO, respectively. Then, an up-scaling optimization procedure and meso-scale FEM homogenization techniques are proposed to link the TES parameters of the atomistic main phases of OPC-based paste and GEO with the homogenized upper meso/macro scale values. To this end, the results of an experimental program on both OPC and GEO pastes have been considered as benchmark to calibrate/validate the numerical tools. Promising simulations at several scales and up-scaling procedures are demonstrated in terms of homogenized temperature-dependent heat capacity and thermal diffusivity, showing a good agreement with the experimental data of the analyzed mixtures.

## 1. Introduction

Energy-efficiency in construction and building materials has become a major challenge for both science and industry [1]. It is driven by the urgent need to strongly reduce the emissions of greenhouse gases and to cut-back on the inefficient usage of the worldwide primary energy. The building stock is actually responsible for over one-third of the global energy consumption and for nearly 40% of total direct and indirect CO2 emissions, making it the largest EU energy consumer [2]. Therefore, a major leap in energy-saving is vital to protect our environment and to boost the EÚs green economy [3,4].

In this attempt, cement-based materials, like concrete, represent the most employed construction materials worldwide. Their basic ingredients match the ones of the Earth's crust and are abundantly available and at low cost [5]. Combining the low-cost nature of cementitious materials, together with the possibility of manipulating their inner multi-scale structures, makes them very attractive for shaping their thermal properties and to achieve highly thermal-energy storage and saving applications, as urgently needed in new and/or existing buildings [6,7].

Despite their practical importance, the origin of the thermal properties of cementitious systems is still at an incipient stage [8]. Most of the existing literature has primarily focused on macroscopic experimental measurements and numerical tools, which have resulted in a loss of connection to the intrinsic properties of the constituents. These studies have mainly concentrated on specific applications such as fire resistance (high temperatures) [9], thermal insulation (mid temperatures) [10], early-age processes

* Corresponding authors.
E-mail addresses: antonio.caggiano@unige.it (A. Caggiano), j.dolado@ehu.eus (J.S. Dolado).

[11], heat exchangers [12], geothermal energy applications [13], and/or studying the effects of special components such as waste glass aggregates and nanosilica [14], micro-encapsulated phase change materials [15], nano-particles [16], etc.

Thermal properties are one-to-one related to the vibrational atomic states, and how these vibrational states are activated as a function of the temperature [17,18]. More specifically, phonons are the physical particles where mechanical vibration is responsible for the transmission of sound and heat [19]. Atomistic simulations can help in understanding how these vibrational modes are excited and predicting valuable parameters like (specific) heat capacity, thermal conductivity and thermal-energy storage parameters in a general sense [20–22].

Nevertheless, until the advent of sufficient computational capacity, the estimation of the Vibrational Density of States (VDOSs) in physics have resorted to simplified models like the Debye model [23] that gives satisfactory results in certain cases. For instance, the Debye model is able to estimate quite well the heat capacity of polycrystalline materials, under low temperature regimes (i.e., temperatures lower than the so-called $T_{Debye}$ temperature). $T_{Debye}$ lies above the room temperature for most of the crystalline phases present in cementitious materials (namely, C2S, C3S or CH). This is the reason why the use of this simple model has been successfully exploited by Bernard et al. [24] to predict the heat capacities of w/c = 0.45 cement paste and the corresponding mortar, measuring a $c_p$ of 870 $J/(kg \times °C)$ for the well-hydrated cement paste and 742 $J/(kg \times °C)$ for the mortar. However, the Debye model is unable to account for the low-energy additional vibrational states of amorphous materials [25], and as anticipated, it falls short in accurately describing the thermal properties when the temperature becomes significant compared to the Debye temperature [26]. In these scenarios, the utilization of precise atomistic simulations becomes indispensable.

In this scenario, the works of Qomi et al. [27] and Zhou et al. [18] have recently disclosed the right theoretical methodology for elucidating the physical origins of thermal properties in cement systems. Indeed, they reported studies of properties of some basic constituents of Ordinary Portland Cement (OPC) pastes (i.e., analysing phases like CH, CSH, C2S and C3S) at room temperatures. As a salient result that directly targets to the limits of Debye model, they noticed the existence of the so-called Boson peak for the CSH gel (see Dolado et al. [28]). This peak, reflected in a deviation with respect to the quadratic frequency dependence of VDOS, is a hallmark in many glassy materials [29], though its origin is still unclear. Dolado [30] has extended the methodology to explore the thermal properties at high temperature, comparing the properties of some crystalline structures present in OPC-based pastes and those made of calcium aluminate cements.

This paper aims to share ongoing work on this topic, reporting new simulations and experiments that have been done for studying the thermal properties of cement-based and alternative binder materials. In particular, based on an extension of the previous work by Dolado [30], this work includes the analysis of temperature-dependent thermal properties of poorly crystalline structures like CSH and NASH. The latter represent the key ingredients of OPC- and geopolymer-based cement pastes, respectively. The heat capacity and thermal conductivity of CSH and NASH have been estimated through atomistic simulations in the temperature range from room temperature (25 °C) till 325 °C. In parallel, some experiments (at both experimental and numerical up-scaling standpoints) on OPC- and geopolymer-based cement pastes have been also carried out for comparative purposes. It is worth mentioning that time-dependent processes, accounting for hydration chemo-mechanics, which can provide representations of nanostructural evolutions at the interchemical-level of single phases, have not

been considered in this proposal and will be part of its future development.

After this general introduction Section, the paper is structured as follows. Section 2 summarizes the experimental tests and data on OPC-based and geopolymer pastes, investigated in this work and used as benchmark for the numerical activities. Section 3 presents the atomistic modelling procedure for analyzing the thermal properties of CSH and NASH structures. They are considered as the key ingredients of OPC- and geopolymer-based cement pastes, respectively. Then, Section 4 discusses the atomistic results while a discussion in Section 5 is provided to link the nano-scale analyses with homogenized (up-) macro-scale results. Then, meso-scale numerical simulations compared against both experimental data, and the homogenized atomistic simulations are presented in Section 6 with the aim to verify the soundness and capabilities of the presented nano-to-meso scale methodology. Finally, some concluding remarks are made in Section 7.

## 2. Experimental tests and data

### 2.1. Materials

Two hydrated pastes were investigated in this work: i) an OPC-based one made of cement (namely, CEM II-42.5R) and ii) a Hybrid Cement (H-Cement, see Martauz et al. [31]), the latter employed for a geopolymer-based paste (with a label GEO). Table 1 and 2 provide the chemical ingredients of the considered binders. They were mixed with distilled water (provided by Sigma–Aldrich Lab and without extra additives) by considering a water-to-cement (binder) ratio of 0.4 and 0.6 by weight, respectively. Specimens were then cast in a cylindrical mold (38 mm diameter × 15 mm height) and sealed. After 24 h, the sample discs were moved to a hermetically closed desiccator, under controlled humidity (i.e., 100 % RH) and kept at 20 °C until they had reached 28 days of curing.

### 2.2. Methods

The samples were tested via differential scanning calorimetry and thermal conductivity procedures after 28 days of curing. They were measured once per test type per temperature level.

#### 2.2.1. Differential scanning Calorimetry

Modulated Differential Scanning Calorimeter (DSC), by using a TA Instrument Q2000, was performed to determine the reversible part of the specific heat of the samples (having weights of 25 mg circa). Aluminum pans were used for all the samples. Measurements were performed with an average heating rate of 3.0 °C/min and amplitude of modulation ± 0.48 °C, with a period of $t_p$ = 60 s. Prior measuring the specific heat values, the test samples were previously pre-heated at 105°C during 1 h. In this way, they have been completely dried allowing the removal of any signals originating from moisture within the grains. This process was carried out within the DSC instrument to avoid the absorption of water from the environment. Finally, data were collected in the temperature range between 50 °C to 300 °C (with an interval step of 50 °C).

#### 2.2.2. Thermal conductivity

LFA 457 Microflash (from NETZSCH Company) was used for determining the thermal diffusivity in all mixtures. Specimens were pellet discs of pastes having a diameter of 10 mm and height of 2 mm (see Fig. 1). These pellets were produced by pressing the powder deriving from the cement paste disc, through by using a hydraulic press and imposing high pressure (of 7 tons circa). The

**Table 1**
Chemical composition of cement CEM II-42.5R.

| Chemical composition [% weight] | SiO$_2$ | Al$_2$O$_3$ | CaO | MgO | SO$_3$ | Na$_2$O | K$_2$O | TiO$_2$ | Fe$_2$O$_3$ |
|---|---|---|---|---|---|---|---|---|---|
| CEM II-42.5R | 19.31 | 4.31 | 61.08 | 2.38 | 2.96 | 0.29 | 0.86 | 0.14 | 2.28 |

**Table 2**
Chemical composition of the H-cement by Martauz et al. [31].

| Chemical composition [% weight] | CaO | SiO$_2$ | Al$_2$O$_3$ | Fe$_2$O$_3$ | MgO | SO$_3$ | K$_2$O | Na$_2$O | L.O.I. |
|---|---|---|---|---|---|---|---|---|---|
| H-Cement | 22.55 | 43.55 | 17.52 | 5.86 | 2.68 | 3.85 | 2.74 | 2.49 | 1.51 |

samples for the measurement of thermal diffusivity were not dried, as possible moisture contents were already avoided during the production of pellets. The samples were spray-coated with graphite, on both sides, in order to enhance light absorption and infrared thermal response. The investigation was carried out at representative temperatures of 25, 100, 200, 300, 400, 500, and 600 °C.

### 2.3. Measurements

The thermal properties of both OPC-based pastes and geopolymers are reported in this section. Particularly, Fig. 2 shows the results in terms of $c_p$ measurements ($J/(g \times° C)$) under rising temperatures. The comparison between OPC-based paste and GEO highlights the fact that the ordinary Portland cement pastes have a lower specific heat capacity, for each level of temperature, than the corresponding GEO data. The behavior of both OPC-based paste and GEO is characterized to have a clear temperature dependency between $c_p$ and the increasing values of the considered temperatures. However the $c_p$ rise (tendentiously linear) is much more evident for the GEO than for the OPC pastes.

Fig. 3 shows the results in terms of thermal diffusivity measurements ($mm^2/s$) at different temperatures. The comparisons between OPC-based paste and GEO show that the OPC ones have quite higher thermal variation, at each T measurements, than the GEO ones. The thermal diffusivity in both OPC-based paste and GEO is characterized to have a rising dependency against the considered temperature levels. This tendency shows a reduction of the thermal diffusivity with a similar trend for both OPC-based paste and GEO.

## 3. Atomistic modelling and nanoscale description

### 3.1. Atomistic structures

This section is paying the attention to CSH and NASH structures, considered as the key ingredients of OPC- and geopolymer-based cement pastes, respectively.
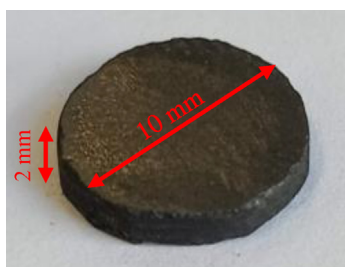


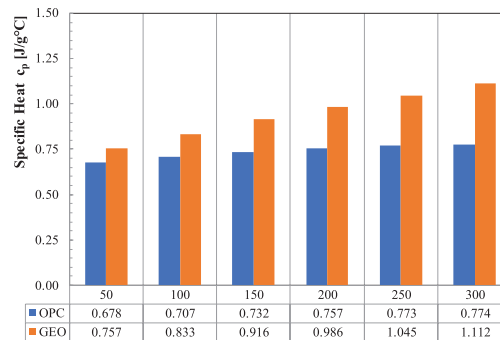**Fig. 1.** Pellet discs of pastes having a diameter d of 10 mm and height h of 2 mm.



| | 50 | 100 | 150 | 200 | 250 | 300 |
|---|---|---|---|---|---|---|
| OPC | 0.678 | 0.707 | 0.732 | 0.757 | 0.773 | 0.774 |
| GEO | 0.757 | 0.833 | 0.916 | 0.986 | 1.045 | 1.112 |

**Fig. 2.** Specific heat of OPC pastes and GEO pastes for several Temp = 50, 100, 150, 200, 250 and 300 °C.



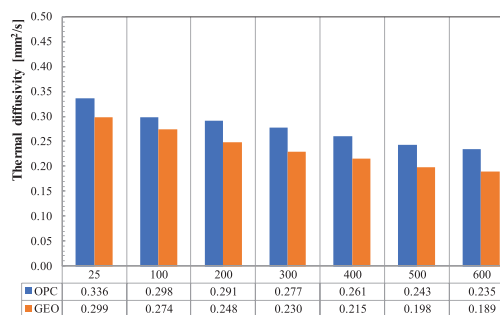| | 25 | 100 | 200 | 300 | 400 | 500 | 600 |
|---|---|---|---|---|---|---|---|
| OPC | 0.336 | 0.298 | 0.291 | 0.277 | 0.261 | 0.243 | 0.235 |
| GEO | 0.299 | 0.274 | 0.248 | 0.230 | 0.215 | 0.198 | 0.189 |

**Fig. 3.** Thermal diffusivities of OPC pastes and GEO pastes for several Temp = 25, 100, 200, 300, 400, 500 and 600 °C.

On the one hand, the structure of CSH is developed according to the procedure described by Qomi et al. [32], based on an improvement of the original procedure proposed by Pellenq et al. [33]. In this context, the structure of Tobermorite 14 Å (with C/S = 0.83) is taken as the starting point (see Fig. 4-a), modifying its structure by firstly removing the water molecules (see Fig. 4-b). Afterwards, some bridging silicate groups are also randomly removed to get the targeted C/S ratio. Finally, to avoid charge unbalances and get the right water content, some Ca-ions and water molecules are randomly added into the inter-laminar space (see Fig. 4-c). The built structure is finally equilibrated by performing an energy minimization and molecular dynamics simulations with the Reactive Force Field (ReaxFF) by Van Duin et al. [34]. Details of ReaxFF and the procedure to construct the CSH model can be found in Duque Redondo [35]. Present study focuses on the C/S = 1.7, which is the average value found in C-S-H gel. The chosen C-S-H configuration actually corresponds to a very large system (an orthogonal cell with sizes a = 26.08 Å, b = 30.84 Å and c = 25.88 Å) and whose exact stoichiometry is $(CaO)_{254}(SiO_2)_{152}(H_2O)_{306}$.

a)

Tobermorite 14 Å

b)

Removing all water and some
bridging silicates. Add Ca$^{2+}$

c)

Reintroducing water. Chemical and
structural relaxation with ReaxFF

**Fig. 4.** The structure of CSH.



a)

Sodalite

b)

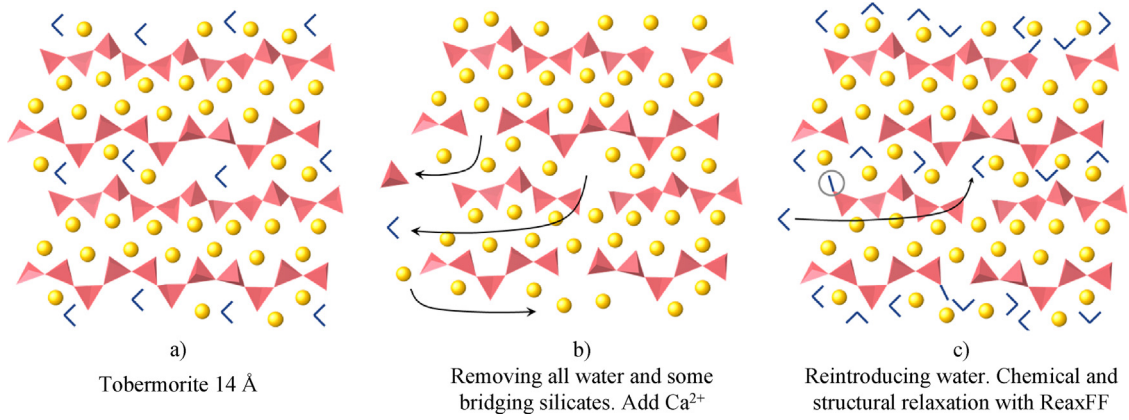Replace CI by ½ Oxygens (or OH)

c)

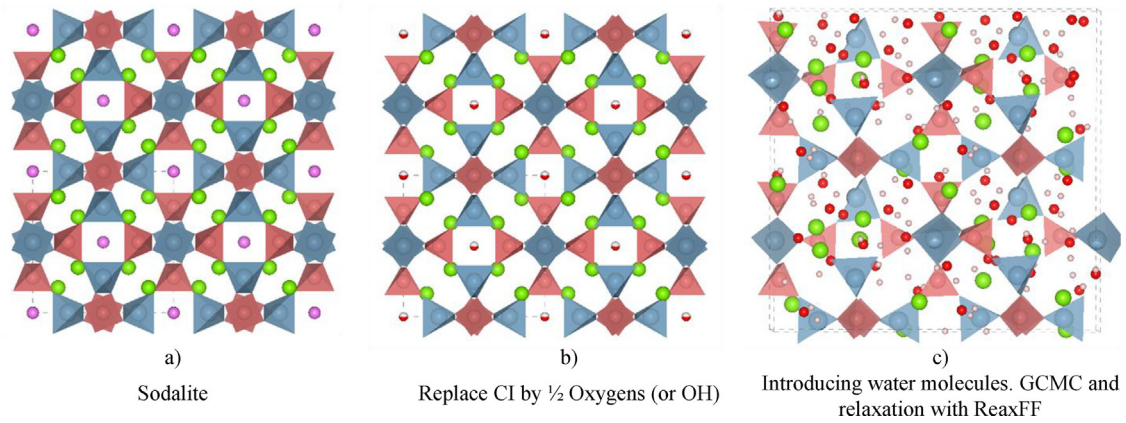Introducing water molecules. GCMC and
relaxation with ReaxFF

**Fig. 5.** The structure of NASH.

On the other hand, a realistic NASH model has been constructed following a protocol akin to the one recently proposed by Lolli et al. [36]. In particular, the starting structure has been the experimental sodalite (Na8 [Al6Si6O24] Cl2), a structure given by Hassan et al. [37] (see Fig. 5-a), to which it has been replaced the Cl atom with an hydroxil ion (see Fig. 5-b). Afterwards, the Gran Canonical Monte Carlo (GCMC) protocol has been applied to introduce water into its structure (see Fig. 5-c). As result, the final structure turned to be $(Na_2O)_4(Al_2O_3)_3(SiO_2)_6(H_2O)_{10}$.

### 3.2. Optimization and relaxation of the structures

The GULP code [38] is used to perform the atomistic calculations. In this approach, the initial structures are optimized to the local energy values that minimise lattice energy, while allowing cell parameters and atomic positions to vary. A quasi–Newton–Rapshon minimisation procedure, i.e. an update of the Hessian variation on the Broyden–Fletcher–Goldfarb–Shannon scheme, is employed. In the case of NASH structure, the GCMC protocol uses a chemical potential of −0.082 eV. The used force field has been the implementation based on Manzano et al. [39] for the ReaxFF. The obtained lattice constants of the CSH and NASH structure can be found in Table 3.

### 3.3. Thermal properties

The heat capacity ($(C)_V$) can be directly extracted from GULP by its definition

**Table 3**
Stoichiometry and lattice constants of the studied CSH and NASH structures.

|  | CSH | NASH |
|---|---|---|
| Composition | $(CaO)_{254}(SiO2)_{152}(H_2O)_{306}$ | $(Na_2O)_4(Al_2O_3)_3(SiO_2)_6(H_2O)_{10}$ |
| a (Å) | 26.08 | 9.53 |
| b (Å) | 30.84 | 9.06 |
| c (Å) | 25.88 | 9.05 |
| $\alpha(°)$ | 90.00 | 92.12 |
| $\beta(°)$ | 90.00 | 90.79 |
| $\gamma(°)$ | 90.00 | 88.45 |

$$(C)_V = \left(\frac{\partial U_{vib}}{\partial T}\right)_V \qquad (1)$$

where

$$U_{vib}(T) = \int_0^\infty \hbar\omega\left(n(\omega) + \frac{1}{2}\right)d\omega \qquad (2)$$

and by plugging the computed VDOS, $g(\omega)$, into $n(\omega) = g(\omega)f_{BE}(\omega, T)$, where

$$f_{BE}(\omega, T) = \left(e^{-\hbar\omega/k_B T} - 1\right)^{-1} \qquad (3)$$

the latter being the so-called Bose–Einstein probability distribution, while the symbol $\omega$ is the angular frequency, $\hbar\omega$ is the phonon energy, $\hbar$ is the reduced Planck's constant, and $k_B$ is the Boltzmann constant. The vibrational density of states does not depend on $T$ (at

the followed harmonic level). In this attempt, the computed VDOS for CSH and NASH gels are shown in Fig. 6.

The thermal conductivity of cement/binder-based materials has been obtained within the framework of lattice dynamics, where the thermal conductivity reads as shown in the following equation

$$k = \frac{1}{V}\sum_i^{3N} C_i(T)D_i \tag{4}$$

being $V$ the cell volume, $C_i(T)$ the heat capacity of the mode $i$ at temperature $T$, $D_i$ the mode diffusivity, and $N$ the number of atoms in the cell volume. While accurate results can be obtained by solving the so-called Boltzmann transport equations for phonons, this work will resort to the Allen-Feldman (AF) theory [40], as it provides reasonable good values at much lower computational costs. Indeed, the validity of AF theory for describing the thermal conductivity of CSH gel, at room temperature, has been proved in [18] where the AF model was benchmarked against the Green–Kubo method within the Equilibrium-MD (EMD) approach. It is worth noting, nevertheless, that anharmonic terms (not included in AF) are expected to be more relevant at higher temperatures when, therefore, the validity of the AF model might be compromised. In any case, a recent study over amorphous silica [41] has shown that the anharmonic contributions, neglected in the AF model, only account for the 25 % of the total thermal conductivity in the range between 125 °C and 525 °C.

In solids, the lattice vibrations are the carriers of heat currents. These lattice vibrations (or modes) can travel long distances (several interatomic distances) when the system is crystalline but quickly decay in space for amorphous and defected materials. In fact, the lack of ordering in amorphous materials implies that the assignment of sensible wave vectors and velocities can be troublesome. In fact, Allen and Feldman [40] found that the normal modes of vibration of amorphous materials naturally segregate into two predominant types of modes called propagons and diffusons. On the one hand, propagons are low frequency modes that exhibit rather identifiable wave vectors and velocities. On the other hand, diffusons are modes that appear to exhibit random vibrations similar to the randomized amorphous structure itself. Localized modes (called locons) can also exist, but their contribution to the thermal conductivity is strictly zero within the harmonic regime approach of the AF model. Therefore, in this work the thermal conductivity is decomposed into two terms, the contribution of the diffusive modes (diffusons) and of propagating modes (propagons). While the first term (namely, diffusive one) can be computed in its totality, the second contribution (i.e., propagating contribution) is only computed above a cut-off frequency, being the low frequency con-

tribution approximated by analytic formulae that describe the quadratic nature of the density of states as it tends to zero frequency.

The contributions from propagating modes are obtained by integrating the results from the Debye model from 0 to $\omega_{AF}$ (the Allen-Feldman cut-off frequency). This relies on finding an approximation to the phonon lifetime as a function of frequency based on the expression

$$\tau = B \times \omega^{-2} \tag{5}$$

from which the propagating contribution to the thermal conductivity can be estimated by means of the equation

$$\kappa_{pr} = 4 \times pi \times k_B \times (c^3) \times B \times \omega_{AF} \times (2/v_s + 1/v_p)/3 \tag{6}$$

where $k_B$ is Boltzmann's constant, $c$ is the speed of light, and $v_s/v_p$ are the velocities of the propagating $s-$ and $p-$waves, respectively. $B$ is a fitting parameter that is found by finding the the maximum peak in Allen-Feldman mode diffusivity below $\omega_{AF}$ and later defining

$$D_{pr}(\omega) = (1/3) \times v_s^2 \times B \times \omega^{-2}. \tag{7}$$

As previously done by Zhou et al. [18] and Dolado [30], an appropriate cut-off frequency has been taken into consideration. By inspecting the VDOS, educated values around 3 THz (precisely 2.99 THz) were taken for both the CSH and NASH gels. Note that below this cut-off frequency, the VDOS (see Fig. 6) scales well with the $v^2$ dependence of the Debye model employed for calculating the contribution of propagons. Moreover, and to avoid size effects when accounting for the low frequency contributions, big simulations cells have been employed ($1 \times 1 \times 1$ and $2 \times 2 \times 1$ supercells for CSH and NASH, respectively).

## 4. Atomistic results and discussion

### 4.1. Heat capacity

In Fig. 7, the specific heat capacities of CSH and NASH structures are plotted as functions of the temperature. It can be seen that the simulated specific heat capacities of NASH phase exceeds those found for CSH phase, capturing well the trend observed in the experimental values measured over OPC-based and GEO pastes, respectively (i.e., as in Fig. 2). This result can be explained in terms of the larger content of water that the NASH structure can host in comparison to the CSH phase.
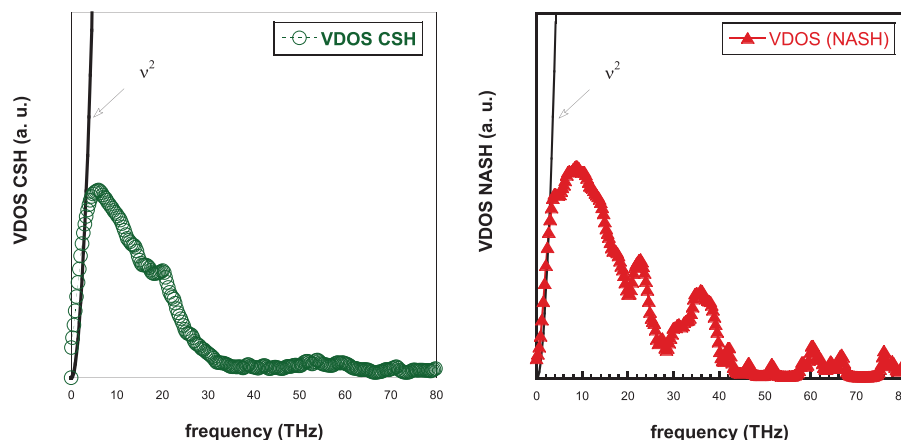


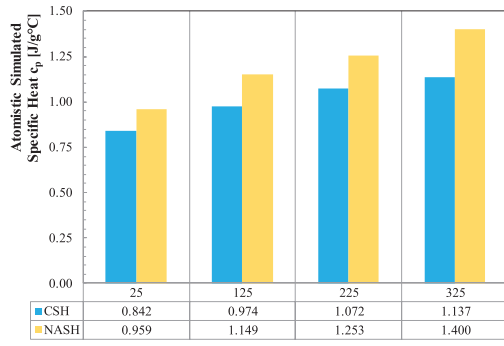**Fig. 6.** VDOS for (a) CSH and (b) NASH gels vs. frequency.

**Fig. 7.** Specific heat of CSH and NASH obtained through atomistic simulations for several Temp = 25, 125, 225 and 325 °C.

*4.2. Thermal diffusivity*

The thermal diffusivity $\lambda$ is defined according to the following equation

$$\lambda = \frac{k}{\rho c_p} \tag{8}$$

being $k$ the conductivity $[W/(m \times° C)]$, $\rho$ is the density $[g/m^3]$, and $c_p$ is the specific heat $[J/(°C \times g)]$.

Firstly, the thermal diffusivities of CSH and NASH phases, arising from the atomistic simulations, are shown in Fig. 8. It can be observed that temperature changes do not sustainably affect the diffusivity, showing only a slight decrease as long as the temperature raises. Moreover, as expected, the thermal diffusivities for the NASH phase are lower than those for the CSH. There is a clear trend: the higher the heat capacity the lower the thermal conductivity and vice versa.

**5. Transition from the atomistic scales to the paste length levels**

*5.1. Proposed approach*

Beyond the knowledge regarding the main phases of OPC-based and GEO pastes (i.e., CSH and NASH, respectively), it is desirable to find other phases (including voids and humidity) that allow to upscale, from the atomistic simulations properties to the experimental macro ones, i.e., the effective diffusivity and specific heat capacity obtained by the experimental procedures explained before.
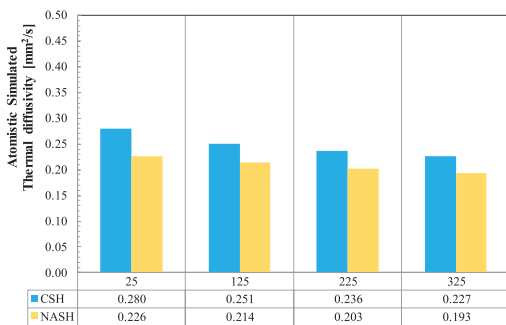


**Fig. 8.** Thermal diffusivities of CSH and NASH obtained through atomistic simulations for several Temp = 25, 125, 225 and 325 °C.

In this sense, the search of the effective properties of these phases is a challenging task, since it is required to find simultaneously different properties, i.e., thermal conductivity, density and specific heat, that in combination with the properties coming from the atomistic simulations, can match the experimental data of the macro scales, i.e., those of the OPC-based and GEO pastes. By choosing appropriate analytical models for the homogenization of these effective properties, and resorting to an optimization procedure, it is proposed to match the previously obtained experimental data with the selected analytical homogenization models. The proposed methodology mainly consists in an iterative process to find a "second generic" phase that best matches simultaneously the experimental diffusivity and the specific heat. In this regard, recourse is made to the simple mixture law [42], to calculate the effective heat capacity per unit volume, while the Maxwell model [43,44] is used to calculate the effective thermal conductivity, and with that, the thermal diffusivity. Further, Genetic Algorithms (GAs) are used to solve the optimization problem. Finally, for a better comparison against the experimental values, the effect of the porosity, together with the rest of the cementitious phases present in the hydrated pastes, is also included in the simulations.

*5.2. Mixture law model*

Under the assumption of no chemical interaction between the components, the effective specific heat of the OPC-based and GEO pastes can be determined as

$$c_{p_{\mathrm{eff}}}^{\mathrm{OPC}} = c_p^{\mathrm{CSH}}(1 - \theta^{\mathrm{2pOPC}}) + c_p^{\mathrm{2pOPC}}\theta^{\mathrm{2pOPC}} \tag{9}$$

and

$$c_{p_{\mathrm{eff}}}^{\mathrm{GEO}} = c_p^{\mathrm{NASH}}(1 - \theta^{\mathrm{2pGEO}}) + c_p^{\mathrm{2pGEO}}\theta^{\mathrm{2pGEO}}, \tag{10}$$

respectively, where the superscript 2pOPC and 2pGEO correspond to the second generic phases that conform the OPC-based and GEO pastes, while $\theta$ represent the mass fraction of these phases.

Since the optimization procedure deals with determining the thermal diffusivity, it is convenient to work in terms of effective heat capacities, and consequently the mixture rule is based on volumetric fractions of each phase. Hence, they can be calculated as

$$C_{\mathrm{eff}}^{\mathrm{OPC}} = \rho c_p^{\mathrm{CSH}}(1 - \phi^{\mathrm{2pOPC}}) + \rho c_p^{\mathrm{2pOPC}}\phi^{\mathrm{2pOPC}} \tag{11}$$

and

$$C_{\mathrm{eff}}^{\mathrm{GEO}} = \rho c_p^{\mathrm{NASH}}(1 - \phi^{\mathrm{2pGEO}}) + \rho c_p^{\mathrm{2pGEO}}\phi^{\mathrm{2pGEO}}, \tag{12}$$

for OPC-based and GEO pastes, respectively; $\phi$ represents the volumetric fraction of the second phases.

Following the same idea, it is also possible to determine the effective density of the composites, i.e.,

$$\rho_{\mathrm{eff}}^{\mathrm{OPC}} = \rho^{\mathrm{CSH}}(1 - \phi^{\mathrm{2pOPC}}) + \rho^{\mathrm{2pOPC}}\phi^{\mathrm{2pOPC}}, \tag{13}$$

and

$$\rho_{\mathrm{eff}}^{\mathrm{GEO}} = \rho^{\mathrm{NASH}}(1 - \phi^{\mathrm{2pGEO}}) + \rho^{\mathrm{2pGEO}}\phi^{\mathrm{2pGEO}}. \tag{14}$$

By combining Eqs. (11)–(14), respectively, it is possible to obtain a new expression for the specific heat in terms of volumetric fraction of the second phase, such as

$$c_{p_{\mathrm{eff}}}^{\mathrm{OPC}} = \frac{C_{\mathrm{eff}}^{\mathrm{OPC}}}{\rho_{\mathrm{eff}}^{\mathrm{OPC}}}, \tag{15}$$

and

$$c_{p_{\mathrm{eff}}}^{\mathrm{GEO}} = \frac{C_{\mathrm{eff}}^{\mathrm{GEO}}}{\rho_{\mathrm{eff}}^{\mathrm{GEO}}}. \tag{16}$$

## 5.3. Maxwell model

Under the same previous assumption of no interaction between components, and considering that the second phase is embedded as spherical particles in a matrix of either CSH or NASH, the effective thermal conductivity can be determined by using the Maxwell model for composite materials, i.e.,

$$k_{\text{eff}}^{\text{OPC}} = k^{\text{CSH}}\left[1 + \frac{3\phi^{2\text{pOPC}}}{\left(\frac{k^{2\text{pOPC}}+2k^{\text{CSH}}}{k^{2\text{pOPC}}-k^{\text{CSH}}}\right) - \phi^{2\text{pOPC}}}\right] \tag{17}$$

and

$$k_{\text{eff}}^{\text{GEO}} = k^{\text{NASH}}\left[1 + \frac{3\phi^{2\text{pGEO}}}{\left(\frac{k^{2\text{pGEO}}+2k^{\text{NASH}}}{k^{2\text{pGEO}}-k^{\text{NASH}}}\right) - \phi^{2\text{pGEO}}}\right]. \tag{18}$$

These equations are only valid for volumetric fraction values less than 0.25 [44].

Once the effective heat capacity and thermal conductivity are determined, it is possible to calculate the corresponding effective thermal diffusivity of OPC-based and GEO composites as

$$\lambda_{\text{eff}}^{\text{OPC}} = \frac{k_{\text{eff}}^{\text{OPC}}}{C_{\text{eff}}^{\text{OPC}}} \tag{19}$$

and

$$\lambda_{\text{eff}}^{\text{GEO}} = \frac{k_{\text{eff}}^{\text{GEO}}}{C_{\text{eff}}^{\text{GEO}}}. \tag{20}$$

## 5.4. Optimization problem

In order to obtain the thermal properties of the second phases, the following constrained optimization problem is solved to minimize the error between the experimental data and the results from the previously defined analytical models, i.e.,

$$\min \quad f(\mathbf{x}) \tag{21}$$

subject to
$$\mathbf{A}\mathbf{x} \leqslant \mathbf{b} \tag{22}$$
$$\mathbf{A}_{\text{eq}}\mathbf{x} = \mathbf{b}_{\text{eq}}, \tag{23}$$
$$\mathbf{l}_b \leqslant \mathbf{x} \leqslant \mathbf{u}_b, \tag{24}$$

where $f$ is the function to be minimized, $\mathbf{x}$ is the vector of design variables, $\mathbf{A}$ and $\mathbf{b}$ are the matrix and vector of inequality constraints, $\mathbf{A}_{\text{eq}}$ and $\mathbf{b}_{\text{eq}}$ the matrix and vector of equality constraints, and $\mathbf{l}_b$ and $\mathbf{u}_b$ the vectors defining the lower and upper bounds of the box constraints, all to be explained below.

### 5.4.1. Design variables

The vector $\mathbf{x}$ is in turn composed of three other vectors containing the thermal conductivity, the specific heat and density, and a scalar defining the volumetric fraction, all representative of the second generic phase, i.e.,

$$\mathbf{x} = [\mathbf{k} \; \mathbf{c}_p \; \boldsymbol{\rho} \; \phi]^{\text{T}}. \tag{25}$$

being $^{\text{T}}$ the transpose vector operator.

The lengths of $\mathbf{k}, \mathbf{c}_p$ and $\boldsymbol{\rho}$ can be selected at will, and depend on the quantity of data to be matched. In the current case, it is desired to match the thermal diffusivity and specific heat (of either OPC-based paste or GEO) at four different temperatures, $T_{\text{eval}} = [25 \; 125 \; 225 \; 325]^{\text{T}}$ expressed in degrees Celsius. By this way, the vector of design variables for the current case of analysis has a length of 13 values and stays as

$$\mathbf{x} = [k^{25}, \dots, k^{325}, c_p^{25}, \dots, c_p^{325}, \rho^{25}, \dots, \rho^{325}, \phi]^{\text{T}}. \tag{26}$$

### 5.4.2. Objective function

The objective function measures the error between the calculated effective diffusivity and specific heat (i.e., from either OPC-based paste or GEO), and the corresponding experimental values (exp), at the four previously defined temperatures, i.e.,

$$f = \left\{ \sum_{i=1}^{N} \frac{0.5}{N} \times \left[ \left(\frac{\lambda_{\text{exp}}^{(i)} - \lambda_{\text{eff}}^{(i)}}{\lambda_{\text{exp}}^{(i)}}\right)^2 + \left(\frac{c_{p_{\text{exp}}}^{(i)} - c_{p_{\text{eff}}}^{(i)}}{c_{p_{\text{exp}}}^{(i)}}\right)^2 \right] \right\}^{1/2}, \tag{27}$$

where the superscript $(i)$ indicates the temperature at which each property is calculated or measured, i.e., the index of vector $T_{\text{eval}}$. The length of this vector is thus equal to four, being $N = 4$.

### 5.4.3. Inequality constraints

These constraints are defined in order to guarantee that $k$ and $c_p$ of the second phase increase (or stay constant) under temperature rises, which means that

$$k^{25} \leqslant k^{125} \leqslant k^{225} \leqslant k^{325}, \tag{28}$$

and

$$c_p^{25} \leqslant c_p^{125} \leqslant c_p^{225} \leqslant c_p^{325}. \tag{29}$$

This hypothesis is based on assuming that properties of the second phase behave like the ones of the CSH and NASH phases (see $c_p$ increasing with temperature in Fig. 7). The latter can be imposed by defining the matrix $\mathbf{A}$ and vector $\mathbf{b}$ (i.e., Eq. (22)) as

$$\mathbf{A} = \begin{bmatrix} 1 & -1 & 0 & 0 & 0 & 0 & 0 & 0 & 0 & 0 & 0 & 0 & 0 \\ 0 & 1 & -1 & 0 & 0 & 0 & 0 & 0 & 0 & 0 & 0 & 0 & 0 \\ 0 & 0 & 1 & -1 & 0 & 0 & 0 & 0 & 0 & 0 & 0 & 0 & 0 \\ 0 & 0 & 0 & 0 & 1 & -1 & 0 & 0 & 0 & 0 & 0 & 0 & 0 \\ 0 & 0 & 0 & 0 & 0 & 1 & -1 & 0 & 0 & 0 & 0 & 0 & 0 \\ 0 & 0 & 0 & 0 & 0 & 0 & 1 & -1 & 0 & 0 & 0 & 0 & 0 \end{bmatrix},$$

and

$$\mathbf{b} = [0 \; 0 \; 0 \; 0 \; 0 \; 0]^{\text{T}}.$$

### 5.4.4. Equality constraints

In this case, the constraints guarantee that the density of the second phase stays constant with changes in the temperature, i.e.,

$$\rho^{25} = \rho^{125} = \rho^{225} = \rho^{325}. \tag{30}$$

To do so, it is defined the matrix $\mathbf{A}_{\text{eq}}$ and the vector $\mathbf{b}_{\text{eq}}$ of Eq. (23) as

$$\mathbf{A}_{\text{eq}} = \begin{bmatrix} 0 & 0 & 0 & 0 & 0 & 0 & 0 & 0 & 1 & -1 & 0 & 0 & 0 \\ 0 & 0 & 0 & 0 & 0 & 0 & 0 & 0 & 0 & 1 & -1 & 0 & 0 \\ 0 & 0 & 0 & 0 & 0 & 0 & 0 & 0 & 0 & 0 & 1 & -1 & 0 \end{bmatrix},$$

$$\mathbf{b}_{\text{eq}} = [0 \; 0 \; 0]^{\text{T}},$$

respectively.

### 5.4.5. Box constraints

These are defined with the intention that the search of the second phase conducts to physical-sound results, i.e., close to typical phase values that can be found for either OPC or GEO pastes. The limits regarding the material properties, i.e., thermal conductivity, density, and specific heat, are selected following the study developed by Qomi et al. [27] of typical phases presented in hydrated OPC-based and GEO pastes. From this work there are identified

the corresponding phases and their min/max property values, i.e., those phases with the lowest thermal conductivity, density and specific heat, and those with the highest values of these variables. In the case of thermal conductivity, close values to the thermal conductivity (in $W/(m \times °C)$) of air and $\beta - C_2S$ (belite) are used for the lower and upper bounds, respectively. For the specific heat (in $J/(kg \times °C)$) close values to those of $C_3S$ (alite) and water were kept. Finally, for the density (in kg/m³), those again of water and alite were taken. Finally, for the volumetric fraction, it is adopted a minimum value of 0.05 and a maximum one of 0.30. Based on this assumption, the vectors for the lower and upper bounds are given as

$$\mathbf{l}_b = [0.026, \ldots, 0.026, 680, \ldots, 680, 1000, \ldots, 1000, 0.05]^T,$$

and

$$\mathbf{u}_b = [3.5, \ldots, 3.5, 4182, \ldots, 4182, 3600, \ldots, 3600, 0.30]^T,$$

respective, with a length of 13 values.

*5.4.6. Optimization solver*

In order to solve the optimization problem (Eqs. (22)–(24)) recourse is made to GAs, which have proven to be robust in solving optimization problems with non-linear objective functions, as it is the case of Eq. (27). For its implementation, it is used the algorithm developed by Deep et al. [45].

For the setting of GAs, the parameters in Table 4 were selected.

*5.5. Results of the proposed approach*

The results of the optimization procedure for the OPC and GEO pastes are those detailed in the Tables 5 and 6, respectively. These second phases are representative of homogenized (smeared) thermal properties of a multi-phase system that could be composed by a blend of alite (C3S), water and air for the OPC pastes, and a blend of calcium silicate hydrate (CSH), water and air for the GEO pastes. With those values it is possible to determine the thermal diffusivity of OPC and GEO pastes by using Eqs. (19) and (20), respectively. As it is depicted in Figs. 9 and 10, the properties of the second generic phases conduct to results that match the experimental data with low error, for both OPC-based paste and GEO. Particularly, the Root Mean Square Errors (RMSEs) in both cases are quite low: $RMSE_{OPC} = 0.61\%$ and $RMSE_{GEO} = 2.54\%$, based on the data plotted in Figs. 9 and 10.

Regarding the specific heat, it is possible to calculate it by using Eqs. (15) and (16). As it is clearly shown in Figs. 11 and 12, the temperature dependency trends and the predicted specific heats are quite good. However, the proposed approach do not exactly match the experimental data, as also evinced by evaluating the RMSEs, employed now upon the data of Figs. 11 and 12 to measure the differences between the predicted values and those experimentally observed: i.e., $RMSE_{OPC} = 17.73\%$ and $RMSE_{GEO} = 6.89\%$, respectively. One of the reasons of this could be that the CSH (or NASH for GEO) presented in the hydrated OPC (or H-cement for GEO) could be different from the one obtained by atomistic simulations.

Also, it can be noticed that the specific heat of the OPC-based paste (or GEO ones) is much lower than the corresponding CSH (or NASH) ones, which it does mean that the second generic phase must have a lower specific heat than the OPC-based paste (or GEO). The latter is directly deducted from the mixture laws of Eqs. (9) and (10), and explains why the optimization procedure, in both cases, leads to results that are close (almost equal) to the lower bounds of the specific heat box constraints. Finally, regarding the optimization results of the volumetric fraction, related to the second generic phase, it is believed that they are in relation to the results of the specific heat. More specifically, since the optimizer cannot choose a lower value than the lower bound for the specific heat, it tries to energetically compensate for this by selecting the highest possible volumetric fraction of the second phases.

## 6. Computational homogenization at the macro-scale

Assumptions and validations of Section 5 are based on the mixture law and Maxwell model. However their soundness and accuracy must be tested, not only against experimental data, but also against more accurate methods based on the homogenization of the effective thermal properties. Regarding the mixture law, it is proven to be an appropriate method for obtaining properties like the effective heat capacity. On the contrary, in the case of the thermal conductivity, the Maxwell model is only valid for volumetric fractions lower than 0.25. As the results of the optimization procedure give values of 0.30 for the volumetric fraction, recourse is made to the Finite Element (FE)-based homogenization technique to obtain the effective thermal conductivity of OPC and GEO pastes, respectively.

By using an ad hoc code in Matlab [46], the FE mesh of the representative volume element (RVE) of OPC-based and GEO pastes is generated. Inside the domain, 50 spheres defining the second phases are randomly distributed. The code has been programmed to control the interpenetration of these spherical inclusions. More specifically, it was configured to reduce at a minimum the merging of the spheres (no interpenetrations were encountered). The thermal conductivities of the phases are those obtained by the optimization procedure of Section 5. Considering an unitary value for the diameter of these spheres, the size of the RVE is iteratively adjusted in order to match the desired volumetric fraction of the inclusions (as also arising from Section 5). In this regard, the size of the RVE is a function of the number of inclusions, i.e., higher the number of spheres, higher the size of the RVE. In order to analyze the effect of the RVE size, microstructures with 25, 50, 75 and 100 spheres were ran, and their effective thermal conductivities calculated. Taking the microstructure with 100 spheres as reference, the maximum obtained error for all the microstructures was less than 0.15%. With this, and because of a matter of computational cost, the RVE with 50 spheres was adopted for all the calculations. Fig. 13 depicts this RVE characterizing the microstructure of either OPC or GEO pastes, showing the second phases in red and the matrix (either CSH or NASH phase) in gray.

The computation homogenization methodology proposed by Yvonnet [47] is used to compute the effective thermal conductivity of the paste whose microstructure is defined by he RVE shown in Fig. 13. Taken this RVE as the domain of analysis $\Omega$, the temperature $\mathbf{T}^{(i)}$ in all the nodes $\mathbf{x}_j \in \Omega$ under a prescribed macroscopic temperature gradient $\mathbf{G}^{(i)} = \mathbf{e}_i$ (where $\mathbf{e}_i, i = 1, 2, 3$ is a canonical vector) is determined by solving the discretized heat conduction equation

$$\mathbf{KT}^{(i)} = \mathbf{0} \tag{31}$$

subject to the periodic boundary conditions

**Table 4**
GA algorithm settings.

| Parameter | Value |
|---|---|
| Number of individuals | 200 |
| Number of generations | 10000 |
| Elite individuals | 5% |
| Selection | Stochastic universal sampling |
| Crossover method | Scattered |
| Crossover probability | 80% |
| Mutation method | Adaptive |

**Table 5**
Parameters arising from the GA optimization procedure for OPC pastes.

| 2nd phase for OPC-based paste modelling | | | | |
|---|---|---|---|---|
| Temp [°C] | k [W/(m·°C)] | $c_p$ [J/(g·°C)] | Density [kg/m³] | Vol. [%] |
| 25 | 0.650 | 0.681 | | |
| 125 | 0.650 | 0.681 | 1883.660 | 30 |
| 225 | 0.660 | 0.681 | | |
| 325 | 0.660 | 0.681 | | |

**Table 6**
Parameters arising from the GA optimization procedure for GEO pastes.

| 2nd phase for GEO modelling | | | | |
|---|---|---|---|---|
| Temp [°C] | k [W/(m·°C)] | $c_p$ [J/(g·°C)] | Density [kg/m³] | Vol. [%] |
| 25 | 0.530 | 0.680 | | |
| 125 | 0.530 | 0.680 | 1165.250 | 30 |
| 225 | 0.530 | 0.680 | | |
| 325 | 0.530 | 0.681 | | |
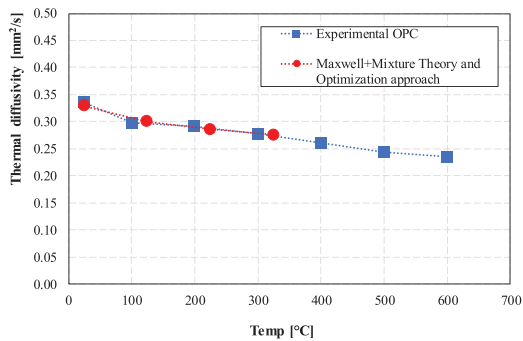


**Fig. 9.** Thermal diffusivity of OPC-based paste: experimental data vs. proposed analytical approach.
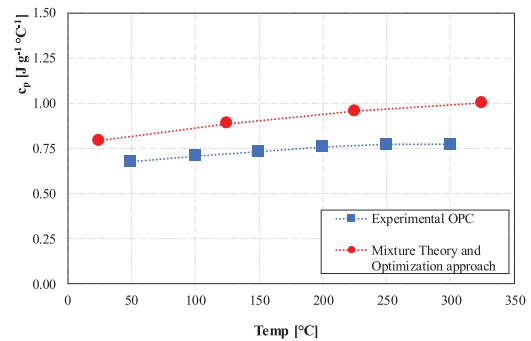


**Fig. 11.** Specific heat of OPC-based paste: experimental data vs. proposed approach.
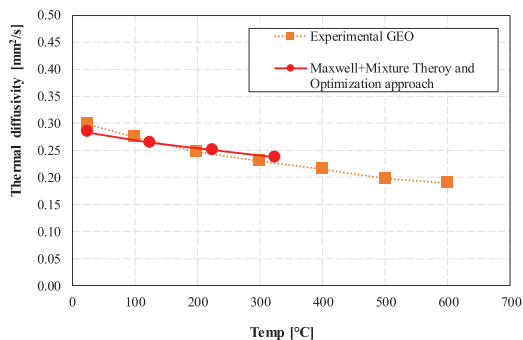


**Fig. 10.** Thermal diffusivity of GEO: experimental data vs. proposed analytical approach.
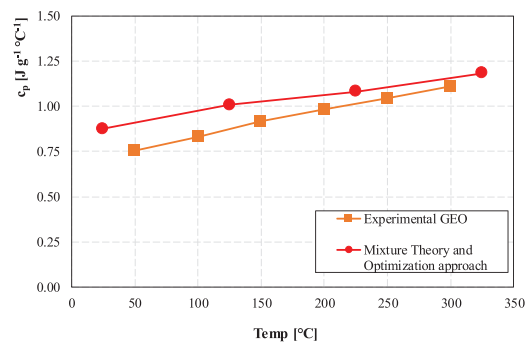


**Fig. 12.** Specific heat of GEO: experimental data vs. proposed approach.

$$T_\alpha^{(i)} - T_\beta^{(i)} = \mathbf{G}^{(i)} \cdot (\mathbf{x}_\alpha - \mathbf{x}_\beta) \tag{32}$$

where **K** is the global conductivity matrix, and $(\mathbf{x}_\alpha, \mathbf{x}_\beta)$ stands for each couple of opposite boundary nodes.

Once $\mathbf{T}^{(1)}$, $\mathbf{T}^{(2)}$, and $\mathbf{T}^{(3)}$ are known, the effective thermal conductivity tensor $\bar{\mathbf{k}}$ is defined by

$$\bar{\mathbf{k}} = \frac{1}{|\Omega|} \int_\Omega \mathbf{k}_\mu \mathbf{B} \begin{bmatrix} \mathbf{T}^{(1)} & \mathbf{T}^{(2)} & \mathbf{T}^{(3)} \end{bmatrix} d\Omega, \tag{33}$$

where $\mathbf{k}_\mu$ is the microscopic thermal conductivity in the RVE, and $B_{ij} = \partial N_j / \partial x_i$, such that $\mathbf{BT} = \nabla T$.

In a previous work of the authors (see Fachinotti et al. [46]), it has been defined a scalar parameter ($\theta_{aniso}$) to evaluate the anisotropy of the thermal conductivity tensor $\bar{\mathbf{k}}$ as

$$\theta_{aniso} = \frac{\max(\bar{k}_{11}, \bar{k}_{22}, \bar{k}_{33})}{\min(\bar{k}_{11}, \bar{k}_{22}, \bar{k}_{33})} - 1, \tag{34}$$

where $\theta_{aniso} \geqslant 0$ and being $\theta_{aniso} = 0$ for isotropic conductivity. For the all analyzed examples of OPC-based and GEO pastes, the highest value of $\theta_{aniso}$ has been evaluated as lower than $1.2 \times 10^{-4}$, which allows to conclude that the observed anisotropy is actually
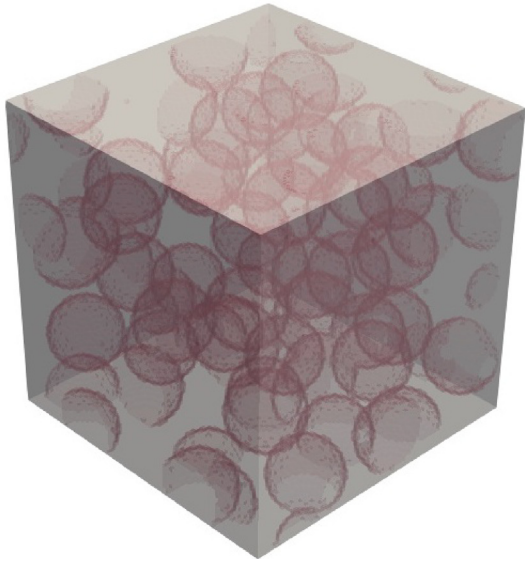
**Fig. 13.** Representative volume element of either OPC or GEO pastes. Red spheres represent the second generic phase embedded in a matrix of CSH or NASH. The volumetric fraction of the second phase is 0.30.
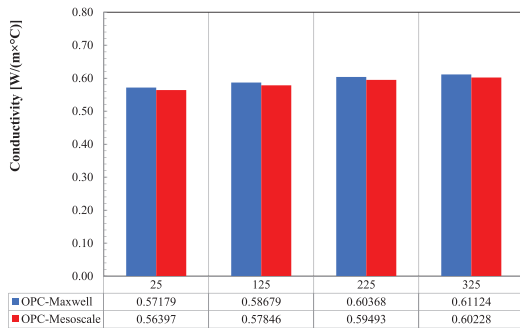


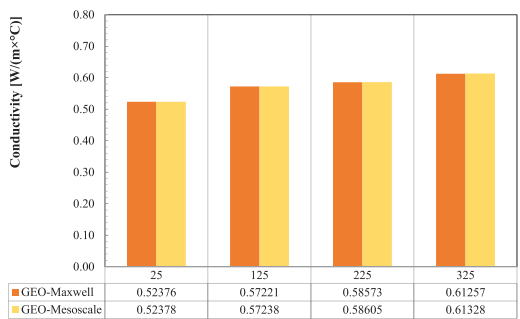**Fig. 14.** Conductivity of OPC-based paste: experimental data vs. meso-scale FEM simulation.



**Fig. 15.** Specific heat of GEO: experimental data vs. meso-scale FEM simulation.

negligible. By this way, it is defined an effective isotropic (scalar) thermal conductivity as

$$k_{\text{eff}} = \frac{\bar{k}_{11} + \bar{k}_{22} + \bar{k}_{33}}{3}. \tag{35}$$

Now, the effective thermal conductivities of OPC and GEO pastes are calculated for the different temperatures, and the results are depicted in Figs. 14 and 15 for OPC-based paste and GEO,

respectively. As it can be appreciated, the FEM results perfectly match the results from the Maxwell models, confirming that the latter approach can be considered appropriate for the determination of the properties of second phases in OPC-based paste and GEO, as well as for the determination of the homogenized thermal energy storage properties of the composites under consideration.

## 7. Concluding remarks

In this work, recent progress on the atomistic description of the thermal properties of cementitious materials, along with some of the concomitant experimental analyses, has been reported. Particularly, two hydrated pastes were investigated, such as an ordinary Portland cement (OPC), and a hybrid cement (an alternative binder called H-Cement) employed for a geopolymer-based paste (GEO).

Based on the achievements and results arising from this work, the following conclusions can be itemized:

- The thermal response of hydrated pastes depends on the thermal activation of vibrational states. In this context, analytical models, like the Debye model, can provide simple descriptions of the vibrations of a solid, though quite satisfactory for (poly) crystalline materials at the low temperature limit (i.e., values much lower than the well-known Debye temperature). However, complex amorphous materials (like CSH and NASH gels) require a more accurate description that is only attainable via atomistic simulations, as shown in this work.
- Heat capacity of CSH and NASH structures have been thus atomistically calculated in a range of temperatures ranging from room temperature to 600 K. Energy minimization and molecular dynamics simulations, by adopting the Reactive Force Field, were performed to regulate the aforementioned structure.
- The atomistic simulations well captured the trend observed in the related experiments, in both over OPC and GEO pastes as well. On one hand, the heat capacity values increase with rising temperature. On the other hand, the NASH structure seems to absorb more heat than the CSH phase.
- By also modelling the thermal diffusivity, it can be stated that the atomistic simulations reproduce quite well the slight decrease of this thermal variable as a function of the temperature. Moreover, contrary to the specific heat capacities, the thermal diffusivities of CSH (and OPC pastes) are larger than those found in NASH (and GEO pastes). Finally, in spite of the crude undertaken approximations, the simulations yield reasonable comparisons with the experimental values.
- Analytical upscaling (i.e., by employing the mixture theory for $c_p$ and $\rho \times c_p$ and Maxwell rules for $k$) and numerical tools (based on meso-scale FEM homogenization) were proposed to link the thermal energy storage parameters of the atomistic phases of OPC and GEO pastes with the homogenized meso/macro scale values.

It is worth highlighting that the homogenization-based FEM procedure was employed to justify the analytical upscaling formulae (i.e., mixture rules and Maxwell model) employed to link the atomistic thermal properties to the upper scales. However, it did not have the aim to validate the results at the atomistic modeling. To identify possible systematic errors that could affect the results of the nanoscale simulations, further studies are needed. Future research will explore the impact of other phases, together with voids and water content, on the vibrational modes and phonon thermal properties of general binder-based composites.

Finally, it is the ambition of the authors to make use of vibration of phonons, atomistic-to-building scale simulations and meta-

optimization tools to achieve nearly-zero conductive media and to use them in designing thermal diodes.

## Data availability

Data will be made available on request.

## Declaration of Competing Interest

The authors declare that they have no known competing financial interests or personal relationships that could have appeared to influence the work reported in this paper.

## References

[1] Bonoli A, Zanni S, Serrano-Bernardo F. Sustainability in building and construction within the framework of circular cities and european new green deal. the contribution of concrete recycling. Sustainability 2021;13 (4):2139.

[2] Tubiello FN, Rosenzweig C, Conchedda G, Karl K, Gütschow J, Xueyao P, et al. Greenhouse gas emissions from food systems: building the evidence base. Environ Res Lett 2021;16(6):065007.

[3] Brøgger M, Wittchen KB. Estimating the energy-saving potential in national building stocks–a methodology review. Renew Sustain Energy Rev 2018;82:1489–96.

[4] Lu S, Fan M, Zhao Y. A system to pre-evaluate the suitability of energy-saving technology for green buildings. Sustainability 2018;10(10):3777.

[5] Scrivener KL. Options for the future of cement. Indian Concr J 2014;88 (7):11–21.

[6] Lizana J, Chacartegui R, Barrios-Padura A, Valverde JM. Advances in thermal energy storage materials and their applications towards zero energy buildings: A critical review. Appl Energy 2017;203:219–39.

[7] Heier J, Bales C, Martin V. Combining thermal energy storage with buildings–a review. Renew Sustain Energy Rev 2015;42:1305–25.

[8] Maddalena R, Roberts JJ, Hamilton A. Can portland cement be replaced by low-carbon alternative materials? a study on the thermal properties and carbon emissions of innovative cements. J Clean Prod 2018;186:933–42.

[9] Achenbach M, Lahmer T, Morgenthal G. Identification of the thermal properties of concrete for the temperature calculation of concrete slabs and columns subjected to a standard fire—smethodology and proposal for simplified formulations. Fire Saf J 2017;87:80–6.

[10] Shahedan NF, Abdullah MMAB, Mahmed N, Kusbiantoro A, Binhussain M, Zailan SN. Review on thermal insulation performance in various type of concrete. AIP Conference Proceedings, vol. 1835. AIP Publishing LLC; 2017. p. 020046.

[11] Honorio T, Bary B, Benboudjema F. Thermal properties of cement-based materials: Multiscale estimations at early-age. Cement Concr Compos 2018;87:205–19.

[12] Kim D, Kim G, Kim D, Baek H. Experimental and numerical investigation of thermal properties of cement-based grouts used for vertical ground heat exchanger. Renew Energy 2017;112:260–7.

[13] Bao X, Memon SA, Yang H, Dong Z, Cui H. Thermal properties of cement-based composites for geothermal energy applications. Materials 2017;10(5):462.

[14] Sikora P, Horszczaruk E, Skoczylas K, Rucinska T. Thermal properties of cement mortars containing waste glass aggregate and nanosilica. Proc Eng 2017;196:159–66.

[15] Jayalath A, Aye L, Ngo T, Mendis P. Multi-scale analysis on thermal properties of cement-based materials containing micro-encapsulated phase change materials. Constr Build Mater 2020;254:119221.

[16] Paul SC, Van Rooyen AS, van Zijl GP, Petrik LF. Properties of cement-based composites using nanoparticles: A comprehensive review. Constr Build Mater 2018;189:1019–34.

[17] Mutisya SM, de Almeida JM, Miranda CR. Molecular simulations of cement based materials: A comparison between first principles and classical force field calculations. Comput Mater Sci 2017;138:392–402.

[18] Zhou Y, Morshedifard A, Lee J, Abdolhosseini Qomi MJ. The contribution of propagons and diffusons in heat transport through calcium-silicate-hydrates. Appl Phys Lett 2017;110(4):043104.

[19] Maldovan M. Sound and heat revolutions in phononics. Nature 2013;503 (7475):209–17.

[20] Gu X, Fan Z, Bao H. Thermal conductivity prediction by atomistic simulation methods: Recent advances and detailed comparison. J Appl Phys 2021;130 (21):210902.

[21] Ávila AF, Donadon LV, Duarte HV. Modal analysis on nanoclay epoxy-based fiber-glass laminates. Compos Struct 2008;83(3):324–33.

[22] Avila AF, Eduardo AC, Neto AS. Vibrational analysis of graphene based nanostructures. Comput Struct 2011;89(11–12):878–92.

[23] Debye P. Zur theorie der spezifischen wärmen. Ann Phys 1912;344 (14):789–839.

[24] Bernard F, Fu J, Kamali-Bernard S. Multiscale modelling approach to determine the specific heat of cementitious materials. Eur J Environ Civil Eng 2019;23 (5):535–51.

[25] Zhou WX, Cheng Y, Chen KQ, Xie G, Wang T, Zhang G. Thermal conductivity of amorphous materials. Adv Funct Mater 2020;30(8):1903829.

[26] Jackson D. Approximate calculation of surface debye temperatures. Surf Sci 1974;43(2):431–40.

[27] Qomi MJA, Ulm FJ, Pellenq RJM. Physical origins of thermal properties of cement paste. Phys Rev Appl 2015;3(6):064010.

[28] Dolado JS, Goracci G, Duque E, Martauz P, Zuo Y, Ye G. Thz fingerprints of cement-based materials. Materials 2020;13(18):4194.

[29] Shibata T, Mori T, Kojima S. Low-frequency vibrational properties of crystalline and glassy indomethacin probed by terahertz time-domain spectroscopy and low-frequency raman scattering. Spectrochim Acta Part A Mol Biomol Spectrosc 2015;150:207–11.

[30] Dolado J. Thermal properties of cement-based materials. In: Proceedings of the Workshop on Concrete Modelling and Materials Behaviour in Honor of Professor Klaas van Breugel. Springer; 2018.

[31] Martauz P, Janotka I, Strigáč J, Bačuvčík M. Fundamental properties of industrial hybrid cement: utilization in ready-mixed concretes and shrinkage-reducing applications. Mater Construcción 2016;66(322). e084–e084.

[32] Qomi M, Krakowiak K, Bauchy M, Stewart K, Shahsavari R, Jagannathan D, et al. Combinatorial molecular optimization of cement hydrates. Nat Commun 2014;5(1):1–10.

[33] Pellenq RJM, Kushima A, Shahsavari R, Van Vliet KJ, Buehler MJ, Yip S, et al. A realistic molecular model of cement hydrates. Proc Nat Acad Sci 2009;106 (38):16102–7.

[34] Van Duin AC, Dasgupta S, Lorant F, Goddard WA. Reaxff: a reactive force field for hydrocarbons. J Phys Chem A 2001;105(41):9396–409.

[35] Duque Redondo E. Atomistic simulations of confined species in 2d nanosructures: clays and csh gel; 2018.

[36] Lolli F, Manzano H, Provis JL, Bignozzi MC, Masoero E. Atomistic simulations of geopolymer models: the impact of disorder on structure and mechanics. ACS Appl Mate Interf 2018;10(26):22809–20.

[37] Hassan I, Antao SM, Parise JB. Sodalite: High-temperature structures obtained from synchrotron radiation and rietveld refinements. Am Mineral 2004;89(2–3):359–64.

[38] Gale JD, Rohl AL. The general utility lattice program (gulp). Mol Simul 2003;29 (5):291–341.

[39] Manzano H, Pellenq RJ, Ulm FJ, Buehler MJ, Van Duin AC. Hydration of calcium oxide surface predicted by reactive force field molecular dynamics. Langmuir 2012;28(9):4187–97.

[40] Allen PB, Feldman JL. Thermal conductivity of disordered harmonic solids. Phys Rev B 1993;48(17):12581.

[41] Zhu X, Shao C. Effect of anharmonicity on the thermal conductivity of amorphous silica. arXiv preprint arXiv:220408165; 2022.

[42] Günther D, Steimle F. Mixing rules for the specific heat capacities of several HFC-mixtures. Int J Refrig 1997;20(4):235–43. https://doi.org/10.1016/s0140-7007(97)00015-7.

[43] Maxwell JC. A treatise on electricity and magnetism, vol. I, 3rd ed. Oxford University Press; 1904.

[44] Pietrak K, Wisniewski T. A review of models for effective thermal conductivity of composite materials. J Power Technol 2015;95(1):14–24.

[45] Deep K, Singh KP, Kansal M, Mohan C. A real coded genetic algorithm for solving integer and mixed integer optimization problems. Appl Math Comput 2009;212(2):505–18. https://doi.org/10.1016/j.amc.2009.02.044.

[46] Fachinotti V, Peralta I, Toro S, Storti B, Caggiano A. Automatic generation of high-fidelity representative volume elements and computational homogenization for the determination of thermal conductivity in foamed concretes. SSRN Electronic J 2022. https://doi.org/10.2139/ssrn.4286262.

[47] Yvonnet J. Computational homogenization of heterogeneous materials with finite elements. Springer International Publishing; 2019. ISBN 3030183823. URL https://www.ebook.de/de/product/36017721/julien_yvonnet_computational_homogenization_of_heterogeneous_materials_with_finite_elements.html.